

Robust Paramagnon and Acoustic Plasmon in a Photo-excited Electron-doped Cuprate Superconductor

Daniel Jost,^{1,*} Jiarui Li,^{1,*} Jordyn Hales,² Jonathan Sobota,¹ Giacomo Merzoni,^{3,4} Leonardo Martinelli,⁴ Shuhan Ding,² Kejun Xu,⁵ Justine Schlappa,³ Andreas Scherz,³ Robert Carley,³ Benjamin E. Van Kuiken,³ Teguh C. Asmara,³ Le Phuong Hoang,³ Laurent Mercadier,³ Sergii Parchenko,³ Martin Teichmann,³ Patrick S. Kirchmann,¹ Giacomo Ghiringhelli,^{4,6} Brian Moritz,¹ Zhi-Xun Shen,^{1,7,5,8} Thomas P. Devereaux,^{1,9,7} Yao Wang,^{2,†} and Wei-Sheng Lee^{1,‡}

¹*Stanford Institute for Materials and Energy Sciences,
SLAC National Accelerator Laboratory, Menlo Park, CA, USA*

²*Department of Chemistry, Emory University, Atlanta, GA 30322, United States*

³*European XFEL, Holzkoppel 4, Schenefeld, 22869, Germany*

⁴*Dipartimento di Fisica, Politecnico di Milano, piazza Leonardo da Vinci 32, I-20133 Milano, Italy*

⁵*Department of Applied Physics, Stanford University, Stanford, CA, USA*

⁶*CNR-SPIN, Dipartimento di Fisica, Politecnico di Milano, I-20133 Milano, Italy*

⁷*Geballe Laboratory for Advanced Materials, Stanford University, Stanford, CA, USA*

⁸*Department of Physics, Stanford University, Stanford, CA, USA*

⁹*Department of Materials Science and Engineering, Stanford University, Stanford, CA, USA*

(Dated: December 1, 2025)

Abstract:

Characterizing the spin and charge degrees of freedom in high-temperature superconducting cuprates under non-equilibrium conditions provides new insights into their electronic correlations. However, their collective dynamics have been largely unexplored due to experimental challenges. Here, we use time-resolved resonant inelastic X-ray scattering (trRIXS) at the Cu L_3 -edge to simultaneously track the collective spin (paramagnon) and charge (acoustic plasmon) dynamics in an optimally electron-doped cuprate driven out-of-equilibrium by a femtosecond pump laser pulse. Upon pumping, we observed an anti-Stokes signal associated with paramagnon generation, which modifies the paramagnon dispersion near the zone center, though the bandwidth remained unchanged, suggesting no significant alteration to spin exchange interactions. Simultaneously, in the charge sector, the acoustic plasmon's energy and spectral weight decreased, suggesting a light-induced redistribution of charge carriers. The variations of both the paramagnon and the plasmon were locked in time, demonstrating a robust intertwining between the spin and charge degrees of freedom on a femtosecond timescale, even in this non-equilibrium state.

MAIN

In high- T_c superconducting cuprates, antiferromagnetic (AFM) correlations and doped charge carriers form a complex and strongly intertwined many-body wavefunction, which can manifest itself as distinct quantum phases by changing doping and temperature [1]. By driving charge and spin degrees of freedom via photoexcitation, the wavefunction could be transiently modified, affecting the electronic properties of cuprates [2] and potentially lead to a state without an equilibrium analog [3–5]. Time-resolved optical spectroscopy [6], angle-resolved photoemission spectroscopy [7], and X-ray scattering [8–12] have elucidated extensive information about the photoexcited response of electronic bands, superconducting pairs, and the lattice, as well as charge order. However, important information, such as the spin super-exchange interaction and the charge density, remain largely unknown. This information can be uniquely deduced from

collective excitations of spin and charge degrees of freedom (see Fig. 1a), which bear the hallmark of the underlying degrees of freedom and can couple to electrons, sculpting electronic properties. Therefore, comprehensive insights into these excitations are essential to portray a complete picture of the photo-excited nonequilibrium state, potentially informing novel strategies for controlling the electronic and magnetic properties of cuprates.

In this regard, resonant inelastic X-ray scattering (RIXS) can be an ideal tool. RIXS has emerged as a powerful tool to probe collective lattice, magnetic, and charge excitations in quantum materials [13, 14]. This technique can be implemented in a pump-probe setting [15, 16] – as time-resolved RIXS (trRIXS) – to track the collective excitations in the time, energy, and momentum domains when the system is driven out-of-equilibrium by femtosecond pump laser pulses. Although the advent of X-ray free-electron laser (FEL) a decade ago has enabled trRIXS measurements [10, 17–20], comprehensive high-resolution trRIXS measurements on cuprates have only recently become possible due to the availability of high-repetition-rate soft X-ray FELs and high-resolution trRIXS instruments.

In this work, we focus on the electron-doped cuprate

* D.J. and J.L. contributed equally to this work.

† yao.wang@emory.edu

‡ leews@stanford.edu

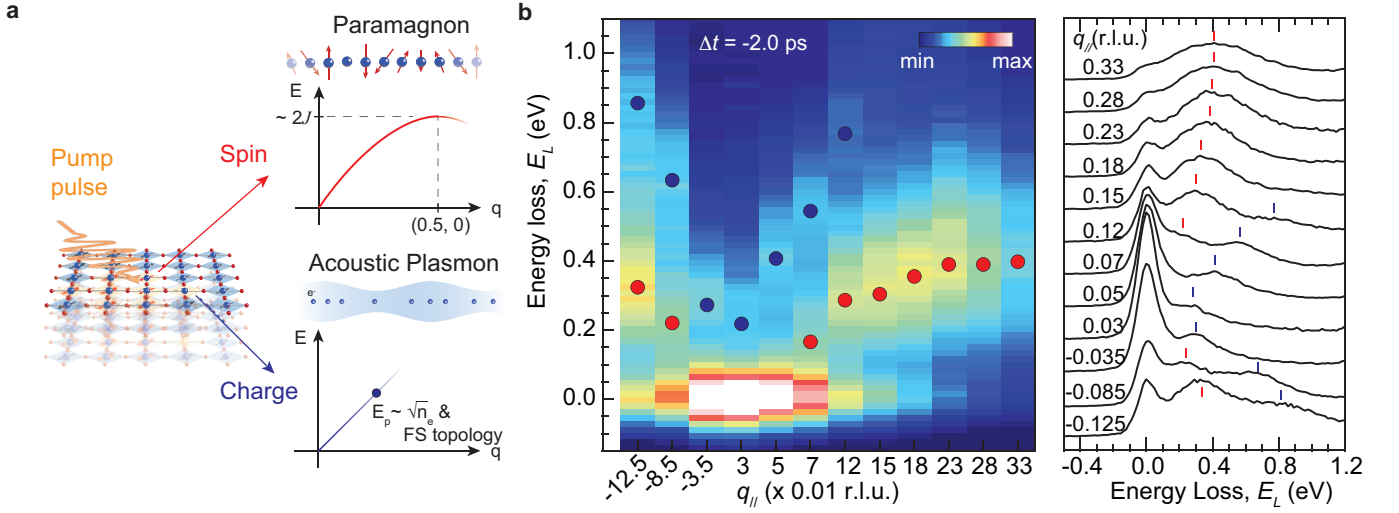


FIG. 1. **Probing the paramagnon and plasmon in an electron-doped cuprate.** **a**, A sketch for information of spin and charge degrees of freedom in a photoexcited cuprate, which can be deduced from paramagnon and acoustic plasmon dispersion. J , E_p , and n_e represent the spin superexchange interaction, plasmon energy at a given momentum, and charge carrier density, respectively. **b**, Energy-momentum RIXS intensity map (left) taken before time zero ($\Delta t = -2.0$ ps). The waterfall plot of RIXS spectra are shown in the right panel. The red and blue markers indicate the paramagnon and plasmon peaks, respectively.

$\text{Nd}_{2-x}\text{Ce}_x\text{CuO}_4$ (NCCO) at the optimal doping $x = 0.15$. At this doping, AFM correlations manifest as short-range spin fluctuations with a correlation length of approximately 20 unit cells [21]. It has been reported that the AFM correlation couples to electrons near the Fermi energy, opening a “hot spot”, back-folding the Fermi surface with respect to the AFM zone boundary [22], and preventing the coherence formation of Cooper pairs [23]. Importantly, distinct from the hole-doped cuprates and many other quantum materials, the electron-doped cuprate NCCO is a unique case where both collective spin (paramagnon) and charge (acoustic plasmon) excitations can be simultaneously detected in the RIXS spectrum [24–26]. This makes it an ideal platform for investigating the interplay of spin and charge in photo-excited non-equilibrium states.

PHOTO-INDUCED PARAMAGNON RESPONSE

We pumped the system with 400 nm laser pulses (see **Methods**). With a photon energy of approximately 3.1 eV, the pump is capable of inducing an electronic transition across the optical charge transfer gap [27], leading to a possible transient modification of the electron-doping concentration at the Fermi level (*i.e.* photo-doping). Simultaneously, the pump’s electric field drives itinerant charge carriers across the short-ranged antiferromagnetic (AFM) background, which impacts the magnetic degrees of freedom. Consequently, a substantial variation in spin and charge collective excitations is anticipated. To characterize these variations, we tracked the time evolution of the paramagnons and plasmons across the Brillouin zone using trRIXS at the Cu L -edge. As a baseline, Fig. 1b

shows RIXS intensity as a function of energy loss E_L and momentum transfer $q_{||}$ along the Cu-O bond direction (*i.e.* the h -direction) taken with X-ray FEL pulses well before the time zero. Dispersive paramagnons are evident, emanating from the zone center ($q_{||} = 0$) toward the zone boundary ($q_{||} = 0.5$) with a bandwidth of approximately 400 meV. Additionally, another branch of rapidly dispersing charge modes, acoustic plasmons [26], can be resolved near the zone center at 0.2 eV. These spectra are consistent with previous static RIXS measurements using the x-rays from synchrotron light sources [24–26].

To evaluate light-driven effects, we analyzed the differential RIXS spectra (Figs. 2a,b), which were obtained by subtracting the spectra at $\Delta t = 0.25$ ps from that at $\Delta t = -2.0$ ps. The variations, particularly the intensity depletion, marked in blue, reflect changes in the spectral line-shape of paramagnons and plasmons across the Brillouin zone, which is accompanied by an apparent increase of the quasi-elastic peak intensity, as marked in red. As a function of time, shown in Fig. 2c for a representative momentum $q_{||} = -0.125$ r.l.u., these spectral variations grow rapidly and reach a maximum at around 0.1 ps – a timescale comparable to our temporal resolution of ~ 0.15 ps – indicating that they are induced mostly during the presence of the pump pulse.

The increase in quasi-elastic peak intensity is somewhat surprising at first glance. Since the energy resolution of the RIXS probe cannot resolve phonons from the quasi-elastic peaks, one might suspect that phonon excitation is responsible for this phenomenon. We argue that this scenario is unlikely. We first note that the photon energy of the pump does not match any phonon energy; therefore, phonons cannot be excited resonantly and can only be indirectly excited through scattering with the

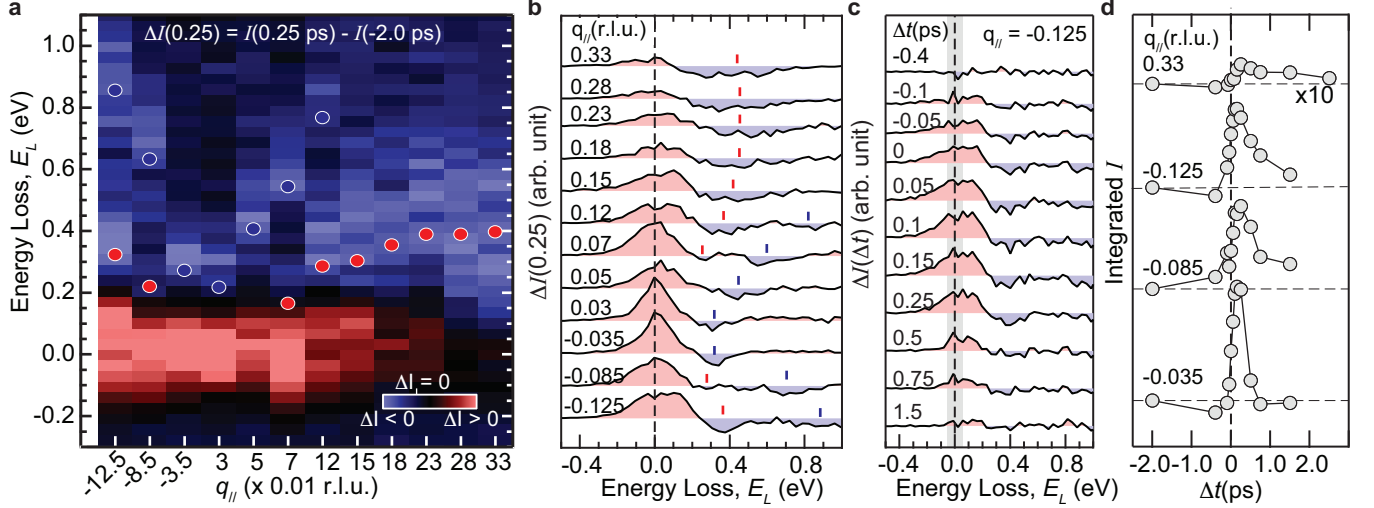


FIG. 2. **Light-driven variations in trRIXS spectra.** **a**, Differential RIXS intensity map obtained by subtracting the RIXS map taken at $\Delta t = 0.25$ ps from that taken at -2.0 ps. The red and blue markers indicated the peak positions of paramagnon and plasmon, same as those shown in Fig. 1b. **b**, Waterfall plot of the differential RIXS spectra shown in panel **a**. The red and blue ticks in the **b** indicate the variations associated near the peaks of paramagnon and plasmon, respectively. **c**, Differential spectral at $q_{||} = -0.125$ r.l.u. taken at different Δt . **d**, Time traces of quasi-elastic peak intensity for four representative $q_{||}$ s, obtained by integrating the intensity within an energy window of ± 60 meV with respect to the zero energy loss, as indicated by the gray shaded area in panel **c**.

photo-excited electronic system, serving as an energy sink for the photo-excited electronic system during its recovery. Therefore, the quasi-elastic peak intensity should continue to grow beyond $\Delta t \sim 0.1$ ps, if the increase is due to the diffused scattering from the increased phonon population. However, this is in stark contrast with our findings that its intensity immediately increases upon pumping, followed by a rapid decrease, as demonstrated in the time traces of the integrated quasi-elastic peak intensity at representative $q_{||}$ s (Fig. 2d). Therefore, the light-enhanced quasi-elastic peak intensity is unlikely to be due to phonons, but rather is associated with the spectral variations of paramagnon and plasmon peaks, which extend into the quasi-elastic region.

Another interesting feature in the differential RIXS spectra is the significant spectral weight in the energy-gain regime (*i.e.* $E_L < 0$). To gain further insight, we examine raw RIXS spectra taken at $q_{||} = 0.33$ r.l.u., a momentum where only the paramagnon excitation is present. As shown in Fig. 3a, the pump broadens the quasi-elastic peak width and enhances the spectral weight in the energy gain regime at least up to $E_L = -0.3$ eV. This indicates the presence of anti-Stokes scattering from certain modes, whose population substantially increases at $\Delta t = 0.25$ ps. The mode, whose energy scales are notably larger than the maximal phonon energy in cuprates (~ 80 meV), are unlikely phonons. Instead, paramagnons are a likely candidate given that they are the dominant mode at this momentum with matching energy scales. We stress that due to the paramagnon's broad peak width (*i.e.* short lifetime), anti-Stokes scattering does not manifest as a distinct peak, but rather as additional spectral

weight in the energy gain (see Extended Data Fig. 2), as observed in our data.

The time evolution of the light-induced paramagnon population can be inferred from Fig. 3b, which displays a time-trace of the integrated energy-gain spectral weight between $E_L = -0.12$ and -0.6 eV (window (i)). We observed a rapid increase in the paramagnon population near time-zero, with a essentially resolution-limited raising time. Following the pump's dissipation, the population declines within a few hundred femtoseconds, reflecting its intrinsic short lifetime in doped systems. In addition to generating paramagnons, the pump also simultaneously reduces the paramagnon peak intensity in the energy loss regime while keeping the peak position unchanged (window (ii) in Fig. 3a). Intriguingly, as shown in the time trace of the integrated paramagnon peak intensity within window (ii) in Fig. 3b, time evolution of the paramagnon peak in $E_L > 0$ essentially follow the light-induced paramagnon population seen in $E_L < 0$.

To investigate whether the paramagnon dispersion is altered by the photo-excitation, we fitted trRIXS spectra to extract the paramagnon peak position as a function of $q_{||}$ at $\Delta t = -2.0$ ps and 0.25 ps, respectively. Given that the paramagnon is overdamped and the evolution of its anti-Stokes and Stokes part of spectrum are locked near the time-zero (Fig. 3b), we approximate the paramagnon spectrum in the photoexcited state with a single Gaussian peak spanning across the zero energy (see also Fig. 2 and Methods). Only the spectra in which the paramagnon peak is distinguishable from the quasi-elastic peak before the time zero ($\Delta t = -2.0$ ps), are fitted. Figure 3c

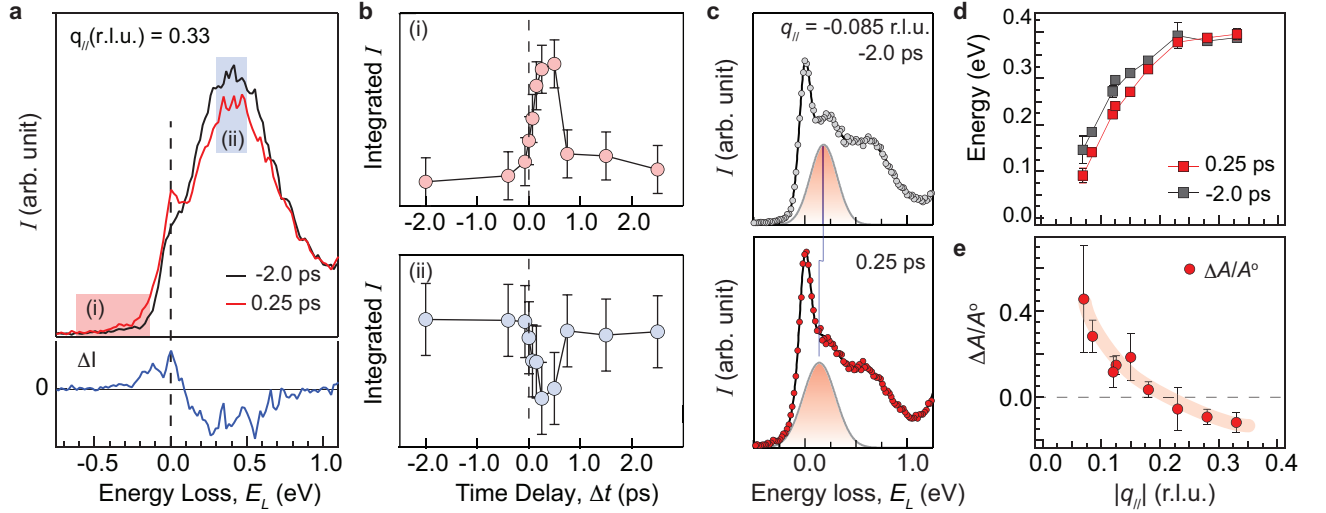


FIG. 3. **Photo-induced variation in Paramagnon.** **a** RIXS spectra at $q_{||} = 0.33$ r.l.u. before and after time-zero with the differential spectrum shown in the lower panel. **b**, Time traces of the integrated intensity within windows (i) and (ii) indicated in panel **a**. The error bars were estimated from the noise level of the RIXS spectrum. **c**, RIXS spectra at a representative momentum near the Brillouin zone center. The fitted paramagnon is shown as the red-shaded area. The vertical line indicates the peak position of the fitted paramagnon excitation. **d**, Summary of the fitted paramagnon positions E_p before (black markers) and after (red markers) time zero. **e** Momentum dependence of the normalized change of the paramagnon spectral weight (area of the fitted paramagnon) $\Delta A = A^{(0.25\text{ps})} - A^o$, where $A^o = A^{(-2.0\text{ps})}$. Shaded area are guide-to-the-eye. The error bars were estimated via standard propagation of uncertainty from the 95% confidence level from the fit of the peak parameter.

shows an example of the fitted paramagnon peak at a representative momentum near the zone center. Interestingly, at $\Delta t = 0.25$ ps, the paramagnon peak position at $q_{||} = -0.085$ r.l.u. appears to soften by $\sim 20\%$, compared to that at $\Delta t = -2.0$ ps. In contrast, at $q_{||} = 0.33$ r.l.u., the peak energy remains unchanged within our experimental uncertainty (Fig. 3a). The distinct behaviors observed at the two momenta point to a momentum-dependent paramagnon softening, as summarized in Figure 3d, which shows the paramagnon dispersion along the h -direction before and after time zero.

Moreover, the light-induced change in paramagnon spectral weight is also momentum-dependent. For all momenta examined here, the paramagnon linewidth increases upon pumping (see Extended Data Fig. 3), reflecting the appearance of light-driven paramagnon in the energy gain via anti-Stokes scattering, and possibly also a shorter lifetime due to light-driven carriers [28, 29]. For small momenta, this light-induced broadening leads to a significant increase in the paramagnon spectral weight, as summarized in Fig. 3e. Interestingly, the enhancement in spectral weight rapidly reduces with increasing momentum and eventually changes sign near $q_{||} \sim 0.2$ r.l.u., beyond which the overall spectral weight begin to decrease during the pump.

Altogether, the pump generates paramagnons, modifies the apparent paramagnon dispersion near the zone center, and redistributes the spectral weight across the Brillouin zone. However, we stress that the dispersion modification does not necessarily imply that the underlying spin exchange interaction is modulated by the pump.

Particularly, in the small $q_{||}$ regime where the energy scale is also smaller, the paramagnon peak position softens mostly due to the substantial anti-Stokes fraction in the overall paramagnon spectral weight (see also Extended Data and Fig. 3 and Fig. 2). In fact, the paramagnon peak position remains unchanged near the zone boundary strongly suggests that the paramagnon dispersion bandwidth remains unchanged by the pump, thereby asserting no alteration in the spin-exchange coupling strength, at least along the h direction measured by our experiment.

UNDERSTANDING SPIN DYNAMICS IN THE PHOTO-EXCITED NON-EQUILIBRIUM STATE

To address the observed light-driven paramagnon variation, we perform time-dependent exact diagonalization simulations for the time-resolved dynamical spin structure factor $S(\mathbf{q}, \omega, \Delta t)$, using the single-band Hubbard model with an electron doping of 16.7%, which is the minimal achievable doping in our cluster calculation (see **Methods**). Pump photon energy and polarization are identical to those used in the experiment. Figs. 4a and b present the $S(\mathbf{q}, \omega, \Delta t)$ calculated using a 12-site at its smallest accessible nonzero momentum $q_{||} = 0.33$ r.l.u. At equilibrium, before the pump pulse arrives, the spectrum exhibits an evident peak at 400 meV corresponding to the paramagnon excitation in NCCO. At the center of the pump ($\Delta t = 0$), this peak height decreases rapidly. At the same time, lower energy spectral weight extending to the energy gain ($\omega < 0$) enhances, manifest as the broad-

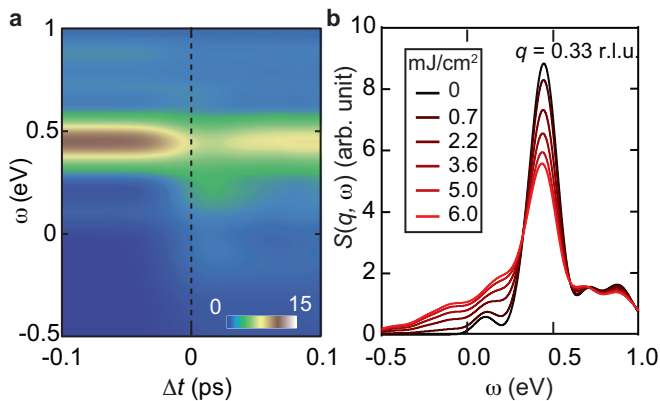


FIG. 4. **Simulated dynamical spin structure factors** $S(q, \omega, t)$. **a**, Time dependence of $S(q, \omega, t)$ at $\mathbf{q} = (0.33, 0)$ for 6 mJ/cm^2 pump, obtained using the single-band Hubbard model. **b**, Fluence dependence of $S(q, \omega, t)$ at the center of the pump ($\Delta t = 0$) for same momentum as panel **a**.

ening of the paramagnon excitation. We also found that the main peak position is essentially unchanged (Fig. 4a) and is insensitive as a function of pump fluence (Fig. 4b). These behaviors of $S(\mathbf{q}, \omega, \Delta t)$ are consistent with our experimental observations. We have also performed trRIXS calculations, which match the behaviors of the calculated $S(\mathbf{q}, \omega, \Delta t)$, ruling out potential artifacts stemming from the finite-core-hole life time and the matrix element effect (Extended Data Fig. 6).

The qualitative agreement between our calculations and the experimental data helps illuminate the mechanism behind the observed light-induced effect. First, in our current geometry, the paramagnons were measured along a momentum direction orthogonal to the pump electric field polarization, which leads to an almost zero Floquet correction to the paramagnon dispersion, unlike the case when the momentum direction is parallel to the pump polarization [29, 30]. Second, the electric field driving the itinerant charge carriers (doublons) across the antiferromagnetic background, scrambling the spin orientation. As a consequence, paramagnons are generated, and the momentum distribution of their spectral weight is also modified (see Extended Data Fig. 7).

COOPERATIVE EVOLUTION OF PARAMAGNON AND ACOUSTIC PLASMON

Lastly, we discuss the response of the collective charge excitation, the acoustic plasmon, in the photo-excited nonequilibrium state. Figures 5a and 5d demonstrate the fit to the spectra taken at $q_{\parallel} = -0.085$ and -0.125 r.l.u., respectively where both paramagnon and plasmon features are resolvable. Interestingly, at both momenta, we observe a light-driven plasmon energy softening across the time zero (Fig. 5b, e), accompanied by spectral weight reduction Fig. 5c, f. The light-driven effect on plasmon could be related to two factors. First, as shown by

trARPES [31], the “hot spots” on the Fermi-surface can be transiently filled via photo-excitation, which alters the Fermi-surface topology, leading to a change of plasmon energy and spectral weight. Additionally, a light-induced charge transfer could be at play, as suggested by recent experiments on a quasi-1D cuprate ladder compound [32] and antiferromagnetic insulator NiO [33]. Particularly, in the case of NiO, an exciton is observed, which is attributed to a light-induced charge transfer from oxygen ligands to Ni sites. Interestingly, recent time-dependent calculations suggest that a similar light-induced charge transfer process could also occur in cuprates [34]. This would decrease the effective charge carrier density on Cu sites, resulting in a decrease of the plasmon energy and spectral weight measured by Cu L -edge RIXS. Unfortunately, deeper insights into this putative photo-induced charge transfer phenomenon requires more complete information about the plasmon dispersion within the three dimensional Brillouin zone and at the O K -edge, which is beyond the scope of the current work.

Intriguingly, as shown in Fig. 5, the time evolution of the paramagnon and plasmon appears to be cooperative: an essentially resolution limited initial change at time zero, reaching their maximal changes at the same time, and then followed by a similar recovery time. This highlight the nature of entangled spin and charge degrees of freedom in doped cuprates: when the system is perturbed, the charges and spins respond collectively and instantly. Such spin-charge intertwining not only exhibits in the thermal equilibrium condition, but also remain robust even when the system is driven out-of-equilibrium, as demonstrated in our work.

DISCUSSION

Our results reveal that the collective excitations of spin and charge—the paramagnon and plasmon—are surprisingly robust against photo-excitation. Based on our experimental parameters and reflectivity measurements at 400 nm, we estimate the average absorbed photon density to be approximately 0.6 photons per unit cell for each pump pulse (see **Methods**). Even with such intense perturbation, while the spectrum are momentarily broadened at time zero, the paramagnon and plasmon dispersions remain well-defined. Another salient observation is the less than anticipated photo-doping effect. This high absorbed excitation density would imply the addition of ~ 0.6 electrons per unit cell (*i.e.*, 60% electron doping) via electronic transitions across the optical charge transfer gap. However, the paramagnon excitations remain well-defined, and their bandwidth shows no significant change. Furthermore, the plasmon’s energy and spectral weight reduce, a behavior opposite to that expected when increasing electron-doping concentration. We note that a less pronounced photo-doping effect has also been reported in photo-excited hole-doped cuprates [29, 35]. These findings further highlight the fundamental

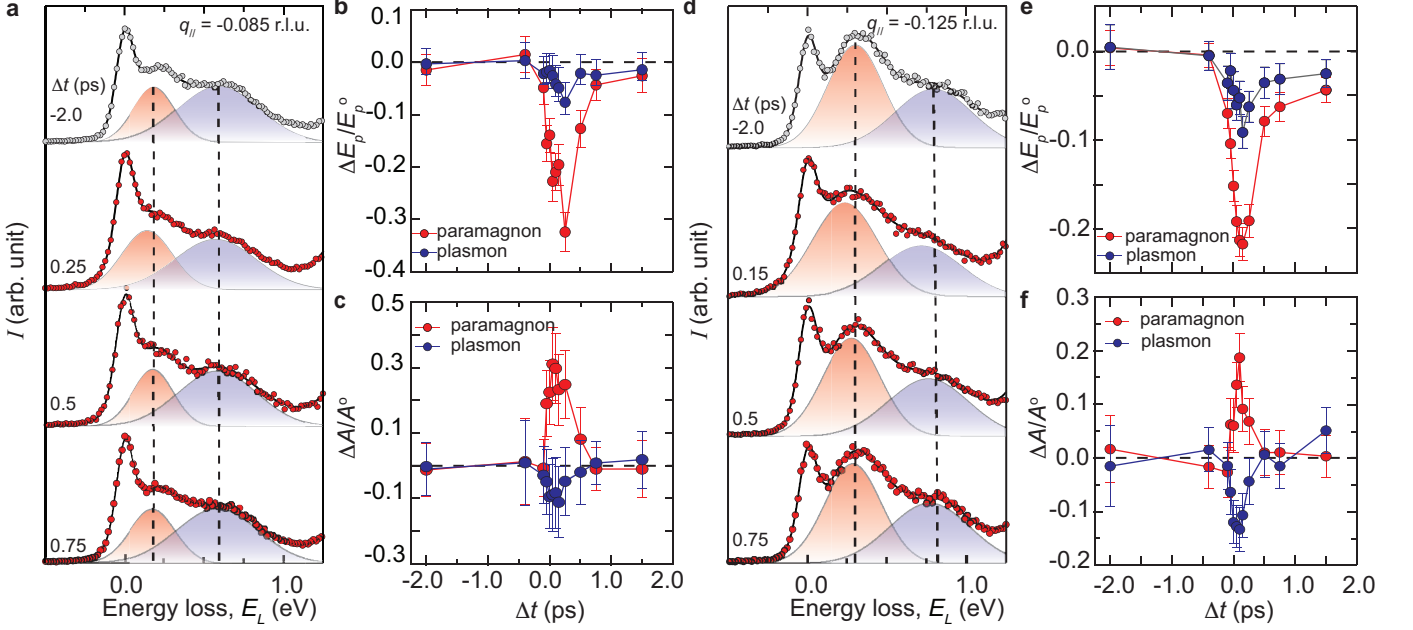


FIG. 5. **Cooperative evolution of paramagnon and plasmon.** **a**, RIXS spectra at representative time delays at $q_{||} = -0.085$ r.l.u.. The red and black shaded peaks represent the fitted paramagnon and plasmon. the dashed lines indicate the peak position before time zero, as guide of lines. **b**, Time traces of normalized peak position changes for paramagnon and plasmon. **c**, Time traces of normalized spectral weight changes for paramagnon and plasmon. **d-f**, Same plots for another momentum at $q_{||} = -0.125$ r.l.u..

differences between photon-doping and chemical-doping in both electron- and hole-doped cuprates.

Nevertheless, ultrafast excitations, as shown in our results, can affect the momentum distribution of the paramagnon and plasmon spectral weight. These bosonic modes effectively couple to electrons and could mediate electronic interactions that could potentially affect the nonequilibrium phases. Looking forward, it would be of great interest to explore advanced photoexcitation schemes that can selectively enhance spectral weight at characteristic large momenta, such as the spin fluctuations at the AFM wave vector (π, π) or charge fluctuations near a charge order wave-vector, potentially opening new pathways for manipulating emergent electronic phases.

On a broader perspective, our results also establish that ultrafast photoexcitation can generate magnetic excitations with non-zero momenta and with significant populations. This capability presents a compelling opportunity for utilizing ultrafast light pulses to excite mobile magnons in future magnonic devices [36], which require efficient magnon excitation and transport. Considering that promising magnetic materials for magnonic applications typically exhibit robust long-range magnetic order and low magnon damping, we anticipate that the light-induced magnons in these systems will possess substantially longer lifetimes than the paramagnons in optimally-doped NCCO, where the magnetic correlations is short ranged.

Author contributions W.S.L and D.J conceived the experiments. D.J., J.L., J.S., L.M., G.M., J.S., A.S., R.C., B.K., T.C.A., L.P.H., L.M., M.T., P.S., G.G. and W.S. conducted the trRIXS experiment. D.L, J.L. and W.S.L analyzed the data. K.X. and Z.X.S. synthesize the NCCO crystals. J.H., S.D., B.M., T.P.D., and Y.W. performed theoretical calculations and accompanying analysis. All authors contributed to the data interpretation. D.J. and W.S.L. wrote the manuscript with input from all authors.

Competing financial interests: The authors declare that there are no competing financial interests.

Data availability statement: Data are available from the corresponding authors upon reasonable request. Data recorded for the experiment at the European XFEL are available at doi:10.22003/XFEL.EU-DATA-003078-00

ACKNOWLEDGMENTS

The Experimental work was supported by the U.S. Department of Energy, Office of Basic Energy Sciences, Materials Sciences and Engineering Division under contract No. DE-AC02-76SF00515. The theoretical simulations (J.H., S.D., and Y.W.) are supported by the U.S. Department of Energy, Office of Science, Basic Energy Sciences, under Early Career Award No. DE-SC0024524. We ac-

knowledge European XFEL in Schenefeld, Germany, for provision of X-ray free-electron laser beamtime at SCS under proposal number 3078 and would like to thank the staff for their assistance. D.J. gratefully acknowledges funding by the Alexander-von-Humboldt foundation. The simulation used resources of the National Energy Research Scientific Computing Center, a U.S. Department of Energy Office of Science User Facility located at Lawrence Berkeley National Laboratory, operated under Contract No. DE-AC02-05CH11231. T.C.A. acknowledges funding from the Heisenberg Resonant Inelastic X-ray Scattering (hRIXS) Consortium.

METHODS

A. Sample synthesis

Single crystals of $\text{Nd}_{1-x}\text{Ce}_x\text{CuO}_4$ ($x = 0.15$, $T_c = 25\text{ K}$) were grown using the floating zone method. The crystals were oriented with Laue. A fresh ab-plane surface was obtained by cleaving in the air right before the experiment.

B. X-ray FEL configuration

The X-ray FEL is operated at the standard pulse train mode with 10 trains per second, 1.1 MHz repetition rate within each train of 360 pulses. The average X-ray pulse energy is 1000 nJ with a pulse duration of 80 fs. For the trRIXS measurement, 90% of the X-ray pulse energy is attenuated to avoid sample heating, while still yielding a strong RIXS signal. The photon energy is tuned to the Cu L -edge for the RIXS measurements. The beam spot on the sample is set to $10\text{ }\mu\text{m}$ (V) \times $150\text{ }\mu\text{m}$ (H).

C. Optical Penetration Depth of the 400 nm Pump Pulses

In order to estimate the penetration of the 400 nm pump laser, we estimate the complex refractive index of NCCO at 15% doping by measuring the angle-dependent reflectivity of 400 nm light for σ - and π -polarizations. We use the frequency-doubled output of a Ti:Sa oscillator at 80 MHz with 100 fs pulse duration and $<38\text{ mW}$ incident power (0.5 nJ pulse energy). NCCO crystals were cleaved and measured in air at room temperature. In this characterization, we estimate the spot size on the sample to be $100\text{ }\mu\text{m}$. At normal incidence, this results in a fluence of 4.2 nJ/cm^2 and a heating power of 335 W/cm^2 , and we assume heating effects to be negligible.

The data and the fitting to determine the index of refraction at 400 nm is shown in Extended Data Fig. 1 b. The data is fit globally by applying the Fresnel equations

to σ - and π -polarized data simultaneously.

$$R_\pi = |r_\pi|^2, r_\pi = \frac{n^2 \cos \alpha_i - \sqrt{n^2 - \sin^2 \alpha_i}}{n^2 \cos \alpha_i + \sqrt{n^2 - \sin^2 \alpha_i}}$$

$$R_\sigma = |r_\sigma|^2, r_\sigma = \frac{\cos \alpha_i - \sqrt{n^2 - \sin^2 \alpha_i}}{\cos \alpha_i + \sqrt{n^2 - \sin^2 \alpha_i}}$$

Where n is the complex index of fraction $n = n + ik$. We obtain $n=1.76(3)$ and $k=0.59(2)$. With $\delta = \frac{\lambda}{4\pi k}$, we arrive at an optical penetration depth of the pump pulse of 400 nm to be 54 nm.

D. trRIXS configurations

The trRIXS measurements were performed at the SCS instrument using the h-RIXS spectrometer [37] with a scattering and pump-probe geometry shown in Extended Data Fig. 1a. The scattering angle is set to be 125° . The samples were mounted on the 6-axis in-vacuum diffractometer and cooled to $\sim 20\text{ K}$. The RIXS data were obtained with incident π polarization (in the scattering plane, high through-put configuration). The incident photon energy was tuned to the maximum of the Cu L_3 -edge X-ray absorption spectrum at $\sim 931\text{ eV}$. The energy resolution was approximately $\Delta E \sim 120\text{ meV}$. The scattering plane coincided with the a-c plane of the crystal with a surface normal along the c-axis. The momentum transfer was calculated using the lattice constants of $a = b = 3.9\text{ }\text{\AA}$ and $c = 12.1\text{ }\text{\AA}$. The scattering geometry is optimized for the paramagnon measurement. Since the paramagnon is quasi-two-dimensional, the RIXS spectra presented here were plotted as a function of in-plane momentum only. In our experiment, we rotate the sample under the collinear pump and probe beams such that theta ranges from 48 to 100 degrees, corresponding to a momentum transfer of q_{parallel} ranging from -0.125 r.l.u to 0.33 r.l.u. Unless otherwise indicated, the RIXS spectra were normalized by the incident photon flux.

Pump pulses with a wavelength of 400 nm and a time duration of 50 fs were used to drive the system. The data shown in the manuscript were taken with a pump fluence of 7 mJ/cm^2 . The total time resolution, estimated to be 150 fs, is a convolution of X-ray FEL jitter, and the x-ray and pump pulse durations. The pump laser spot size was set to $120\text{ }\mu\text{m}$ (V) \times $300\text{ }\mu\text{m}$ (H), which is substantially larger than the x-ray spot on the sample, ensuring homogeneous photon excitation within the probed region. The pump beam and x-ray beam were collinear before they reached the sample. The polarization of the pump laser was set to be perpendicular to the scattering plane, such that the relative orientation between the pump polarization and the crystalline axis of the sample remained unchanged when we rotated the sample angle for different momentum positions. The pump power was adjusted for different sample angles so that the pump fluence was kept fixed at 7 mJ/cm^2 .

We can estimate the 400 nm pump excitation density within the XFEL probe beam footprint using our

experimental parameters and the reflectivity data (Extended Data Fig. 1b). Reflectivity measurements for the σ -polarized pump laser, averaged over the experimental sample angles, yielded a value of approximately 0.2. This corresponds to an absorption coefficient of 0.8 and a pump penetration depth of approximately 50 nm (Methods, previous section). Based on these values, we estimate an absorption of approximately 0.6 photons per unit cell per pulse.

E. Fitting of RIXS spectrum

All the RIXS data were normalized to incident photo flux. For each time delay and momentum position, the zero-energy-loss position were determined by the fitted elastic peak position. The fitting model involve a Voigt function for the elastic peak with a full width half maximum of ~ 0.12 eV and a Gaussian-Lorentzian factor of ~ 0.2 , corresponding to the instrument resolution. The paramagnon and the acoustic plasmon were modeled using Gaussian functions. Since both paramagnon and plasmon are notably broader than the instrument resolution (~ 0.12 eV), we did not deconvolve the instrument resolution from the fitted Gaussian peaks. In addition, a tail of Lorentzian is used to account for the for high energy background arisen from the dd excitations. We note that while it is generally assumed an odd function with respect to the zero energy, such as the anti-Lorentzian function or the damped harmonic oscillator function, to fit the magnetic excitation in RIXS, this assumption is only valid for static RIXS spectrum at low temperature. Because in the low temperature equilibrium state, the anti-Stoke scattering effect can be neglected, and thus the dynamical structure factor measured by RIXS can be approximated by the magnetic susceptibility, which possesses an odd parity. In the presence of a significant population of magnons, the dynamical structure factor can no longer be approximated as the susceptibility and a simple functional form is still not available. While in the thermal equilibrium condition, the dynamical structure can be related to susceptibility via dissipation-fluctuation theorem, such relation is not valid in the photo-excited nonequilibrium state. Therefore, we adopted the simplest model to fit the paramagnon and plasmon with a Gaussian by allowing the peak to cross the zero energy (see Extended Data Fig. 2).

F. Single-Band Hubbard Model

We use the single-band Hubbard model Hamiltonian to simulate the NCCO system, whose Hamiltonian is

$$\begin{aligned} \mathcal{H} = & -t_h \sum_{\langle i,j \rangle \sigma} [c_{i\sigma}^\dagger c_{j\sigma} + \text{H.c.}] - t'_h \sum_{\langle\langle i,j \rangle\rangle \sigma} [c_{i\sigma}^\dagger c_{j\sigma} + \text{H.c.}] \\ & + U \sum_i n_{i\uparrow} n_{i\downarrow}, \end{aligned} \quad (1)$$

where $c_{i\sigma}$ ($c_{i\sigma}^\dagger$) annihilates (creates) a valence electron and $n_{i\sigma} = c_{i\sigma}^\dagger c_{i\sigma}$ is the number operator. The valence electrons form a single band with nearest-neighbor hopping amplitude t_h , next nearest-neighbor hopping amplitude t'_h , and on-site Coulomb repulsion U . The parameters are chosen as $U = 8t_h$, $t'_h = -0.3t_h$, and $t_h = 400$ meV, following Ref. 38.

For pump-probe simulations, we employ a 12-site cluster to simulate pump-probe spectroscopes, where the doping is set as 16.7% electron doping, the minimal doping level in this finite cluster with SU(2) symmetry. These simulations assume zero temperature and their the ground-state wavefunctions $|\Psi_G\rangle$ are obtained using the parallel Arnoldi method [39, 40]. For equilibrium finite-temperature simulations, a larger 6×6 cluster is used.

G. Pump-Probe Simulations by ED

The light-matter interaction is described through the Peierls substitution $t_h c_{i\sigma}^\dagger c_{j\sigma} \rightarrow t_h e^{i \int_{\mathbf{r}_i}^{\mathbf{r}_j} \mathbf{A}(t) \cdot d\mathbf{r}} c_{i\sigma}^\dagger c_{j\sigma}$. During the presence of the laser pulse, the vector potential $\mathbf{A}(t)$ gives time dependence to the many-body Hamiltonian in Eq. (1), denoted as $\mathcal{H}(t)$. To mimic the pump-probe experiment, we simulate the pump pulse with an oscillatory Gaussian vector potential:

$$\mathbf{A}(t) = A_0 \hat{e}_{\text{pol}} \exp \left[-\frac{(t-t_0)^2}{2\sigma^2} \right] \cos(\Omega t), \quad (2)$$

and fix the polarization as $\hat{e}_{\text{pol}} = \hat{x}$ and the pump frequency as $\Omega = 3.1$ eV. The time evolution of the wavefunction with the presence of a laser field $|\Psi_e(t + \delta t)\rangle \approx e^{-i\mathcal{H}(t)\delta t} |\Psi_e(t)\rangle$ through the Krylov subspace technique [41].

To describe the evolution of paramagnon excitations, we simulate the nonequilibrium dynamical spin structure factor. It is obtained through the integral of two-time correlations

$$\begin{aligned} \mathcal{S}(q, \omega, t) = & \frac{1}{N} \iiint dt_1 dt_2 e^{i\omega(t_2-t_1)} g(t_1; t) g(t_2; t) \\ & \times \langle \Psi(t_2) | \rho_{-\mathbf{q}}^{(\text{spin})} \rho_{\mathbf{q}}^{(\text{spin})} | \Psi(t_1) \rangle. \end{aligned} \quad (3)$$

Here, the $g(\tau; t)$ is a probe shape function at time t , taken as Gaussian $\exp[-(\tau-t)^2/2\sigma_{\text{pr}}^2]/\sqrt{2\pi\sigma_{\text{pr}}}$ in this work. The momentum-representation spin excitation operator is defined as $\rho_{\mathbf{q}}^{(\text{spin})} = \sum_i (n_{i\uparrow} - n_{i\downarrow}) e^{i\mathbf{r}_i \cdot \mathbf{q}}$.

We also present the trRIXS simulation in the SI, as a more faithful description of the experimental settings. By explicitly considering the X-ray scattering processing, involving an intermediate core level (specifically the $2p$ orbitals of Cu in the L -edge RIXS), the full Hamiltonian reads as

$$\begin{aligned} \mathcal{H}' = & \mathcal{H} + \sum_{i\alpha\sigma} E_{\text{edge}} (1 - n_{i\alpha\sigma}^{(p)}) - U_c \sum_{i\alpha\sigma'} c_{i\sigma}^\dagger c_{i\sigma} (1 - n_{i\alpha\sigma'}^{(p)}) \\ & + \lambda \sum_{i\alpha\sigma'} p_{i\alpha\sigma}^\dagger \chi_{\alpha\alpha'}^{\sigma\sigma'} p_{i\alpha'\sigma'}. \end{aligned} \quad (4)$$

Here, the $p_{i\alpha\sigma}$ ($p_{i\alpha\sigma}^\dagger$) annihilates (creates) a core-level $2p_\alpha$ electron ($\alpha = x, y, z$) and $n_{i\alpha\sigma}^{(p)} = p_{i\alpha\sigma}^\dagger p_{i\alpha\sigma}$ are the core-level electron density operators. The core-hole potential U_c is instead fixed at $4t_h$ and regarded identical for all $2p$ orbitals [38]. $E_{\text{edge}} = 938 \text{ eV}$ represents instead the Cu L -edge absorption energy, i.e., the energy difference between the $3d$ and $2p$ orbitals without spin-orbit coupling. Finally, the spin-orbit coupling with the X-ray-induced core hole in the degenerate $2p$ -orbitals is accounted by the last term in Eq. (4) with $\lambda = 13 \text{ eV}$ [42, 43].

The trRIXS cross-section reads as [29]

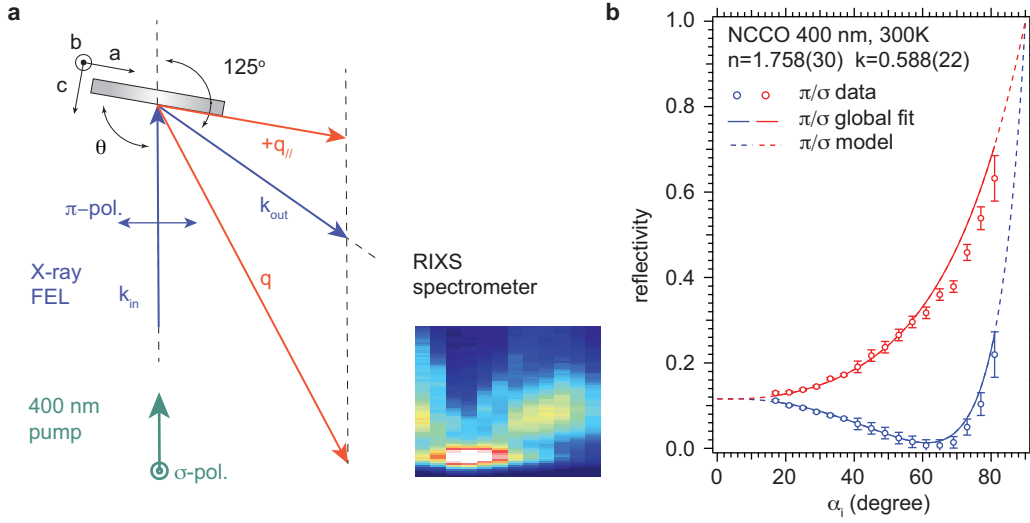
$$\begin{aligned} \mathcal{I}(q, \omega_s, \omega_i, t) = & \frac{1}{2\pi N} \iiint dt_1 dt_2 dt'_1 dt'_2 e^{i\omega_i(t_2-t_1) - i\omega_s(t'_2-t'_1)} \\ & \times g(t_1; t) g(t_2; t) l(t'_1 - t_1) l(t'_2 - t_2) \\ & \times \langle \hat{D}_{q_i \varepsilon_i}^\dagger(t_2) \hat{D}_{q_s \varepsilon_s}(t'_2) \hat{D}_{q_s \varepsilon_s}^\dagger(t'_1) \hat{D}_{q_i \varepsilon_i}(t_1) \rangle \end{aligned} \quad (5)$$

where $q = \mathbf{q}_i - \mathbf{q}_s$ ($\omega = \omega_i - \omega_s$) is the momentum (energy) transfer between incident and scattered photons, and $l(t) = e^{-t/\tau_{\text{core}}} \theta(\tau)$ the core-hole decay lifetime. For a direct transition, the dipole operator reads as $\mathcal{D}_{\mathbf{q}\varepsilon} = \sum_{i\alpha\sigma} e^{-i\mathbf{q}\cdot\mathbf{r}_i} (M_{\alpha\varepsilon} c_{i\sigma}^\dagger p_{i\alpha\sigma} + h.c.)$. We further select combination of π - σ polarizations for incident and scattering photons to maximize the contributions from the spin-flip process [38, 44–47].

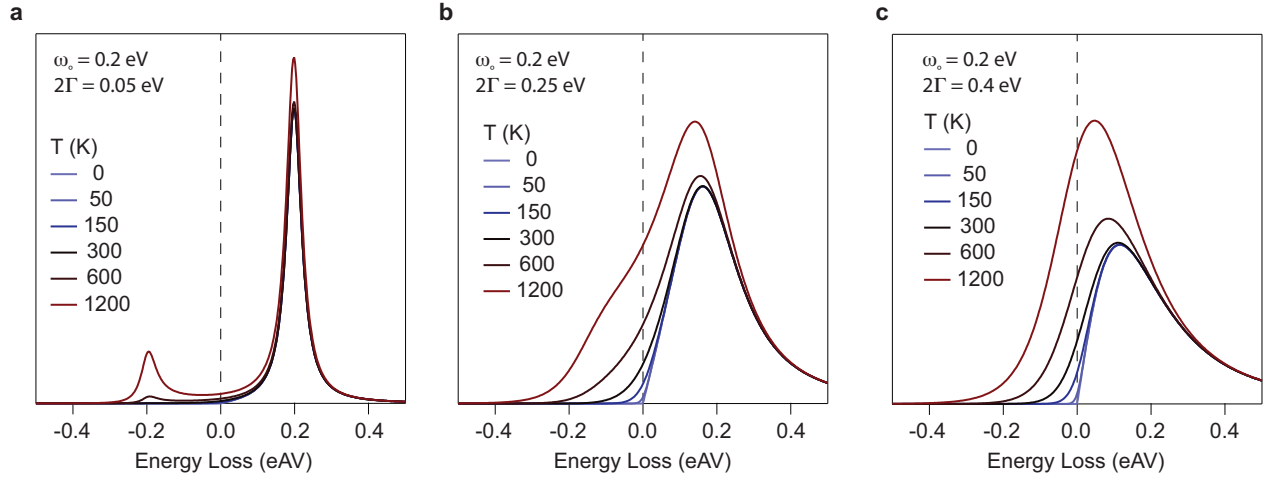
-
- [1] B. Keimer, S. A. Kivelson, M. R. Norman, S. Uchida, and J. Zaanen, From quantum matter to high-temperature superconductivity in copper oxides, *Nature* **518**, 179 (2015).
- [2] D. N. Basov, R. D. Averitt, and D. Hsieh, Towards properties on demand in quantum materials, *Nature Materials* **16**, 1077 (2017).
- [3] Y. H. Wang, H. Steinberg, P. Jarillo-Herrero, and N. Gedik, Observation of floquet-bloch states on the surface of a topological insulator, *Science* **342**, 453 (2013), <https://www.science.org/doi/pdf/10.1126/science.1239834>.
- [4] Y. Wang, M. Claassen, C. D. Pemmaraju, C. Jia, B. Moritz, and T. P. Devereaux, Theoretical understanding of photon spectroscopies in correlated materials in and out of equilibrium, *Nature Reviews Materials* **3**, 312 (2018).
- [5] A. de la Torre, D. M. Kennes, M. Claassen, S. Gerber, J. W. McIver, and M. A. Sentef, Colloquium: Nonthermal pathways to ultrafast control in quantum materials, *Rev. Mod. Phys.* **93**, 041002 (2021).
- [6] C. Giannetti, M. Capone, D. Fausti, M. Fabrizio, F. Parmigiani, and D. Mihailovic, Ultrafast optical spectroscopy of strongly correlated materials and high-temperature superconductors: a non-equilibrium approach, *Advances in Physics* **65**, 58 (2016), <https://doi.org/10.1080/00018732.2016.1194044>.
- [7] M. Zonno, F. Boschini, and A. Damascelli, Time-resolved arpes on cuprates: Tracking the low-energy electrodynamics in the time domain, *Journal of Electron Spectroscopy and Related Phenomena* **251**, 147091 (2021), <https://www.science.org/doi/pdf/10.1126/science.abd7213>.
- [8] R. Mankowsky, A. Subedi, M. Först, S. O. Mariager, M. Chollet, H. T. Lemke, J. S. Robinson, J. M. Glowinski, M. P. Minitti, A. Frano, M. Fechner, N. A. Spaldin, T. Loew, B. Keimer, A. Georges, and A. Cavalleri, Non-linear lattice dynamics as a basis for enhanced superconductivity in $\text{YBaCuO}_{6.5}$, *Nature* **516**, 71 (2014).
- [9] M. Först, R. I. Tobey, H. Bromberger, S. B. Wilkins, V. Khanna, A. D. Caviglia, Y.-D. Chuang, W. S. Lee, W. F. Schlotter, J. J. Turner, M. P. Minitti, O. Krupin, Z. J. Xu, J. S. Wen, G. D. Gu, S. S. Dhesi, A. Cavalleri, and J. P. Hill, Melting of charge stripes in vibrationally driven $\text{La}_{1.875}\text{Ba}_{0.125}\text{CuO}_4$: Assessing the respective roles of electronic and lattice order in frustrated superconductors, *Phys. Rev. Lett.* **112**, 157002 (2014).
- [10] M. Mitrano, S. Lee, A. A. Husain, L. Delacretaz, M. Zhu, G. de la Peña Muñoz, S. X.-L. Sun, Y. I. Joe, A. H. Reid, S. F. Wandel, G. Coslovich, W. Schlotter, T. van Driel, J. Schneeloch, G. D. Gu, S. Hartnoll, N. Goldenfeld, and P. Abbamonte, Ultrafast time-resolved x-ray scattering reveals diffusive charge order dynamics in $\text{La}_{2-x}\text{Ba}_x\text{CuO}_4$, *Science Advances* **5**, eaax3346 (2019), <https://www.science.org/doi/pdf/10.1126/sciadv.aax3346>.
- [11] H. Jang, S. Song, T. Kihara, Y. Liu, S.-J. Lee, S.-Y. Park, M. Kim, H.-D. Kim, G. Coslovich, S. Nakata, Y. Kubota, I. Inoue, K. Tamasaku, M. Yabashi, H. Lee, C. Song, H. Nojiri, B. Keimer, C.-C. Kao, and J.-S. Lee, Characterization of photoinduced normal state through charge density wave in superconducting $\text{YBa}_2\text{Cu}_3\text{O}_{6.67}$, *Science Advances* **8**, eabk0832 (2022), <https://www.science.org/doi/pdf/10.1126/sciadv.abk0832>.
- [12] S. Wandel, F. Boschini, E. H. da Silva Neto, L. Shen, M. X. Na, S. Zohar, Y. Wang, S. B. Welch, M. H. Seaberg, J. D. Koralek, G. L. Dakovski, W. Hettel, M.-F. Lin, S. P. Moeller, W. F. Schlotter, A. H. Reid, M. P. Minitti, T. Boyle, F. He, R. Sutarto, R. Liang, D. Bonn, W. Hardy, R. A. Kaindl, D. G. Hawthorn, J.-S. Lee, A. F. Kemper, A. Damascelli, C. Giannetti, J. J. Turner, and G. Coslovich, Enhanced charge density wave coherence in a light-quenched, high-temperature superconductor, *Science* **376**, 860 (2022), <https://www.science.org/doi/pdf/10.1126/science.abd7213>.
- [13] L. J. P. Ament, M. van Veenendaal, T. P. Devereaux, J. P. Hill, and J. van den Brink, Resonant inelastic x-ray scattering studies of elementary excitations, *Rev. Mod. Phys.* **83**, 705 (2011).
- [14] M. Mitrano, S. Johnston, Y.-J. Kim, and M. P. M. Dean, Exploring quantum materials with resonant inelastic x-ray scattering, *Phys. Rev. X* **14**, 040501 (2024).
- [15] D. Jost, E. G. Lomeli, T. Tang, J. J. Kas, J. J. Rehr, W.-S. Lee, H.-C. Jiang, B. Moritz, and T. P. Devereaux, Time-Resolved X-Ray Spectroscopy from the Atomic Orbital Ground State Up, *Phys. Rev. X* **15**, 011012 (2025).

- [16] M. Mitrano and Y. Wang, Probing light-driven quantum materials with ultrafast resonant inelastic x-ray scattering, *Communications Physics* **3**, 184 (2020).
- [17] M. P. M. Dean, Y. Cao, X. Liu, S. Wall, D. Zhu, R. Mankowsky, V. Thampy, X. M. Chen, J. G. Vale, D. Casa, J. Kim, A. H. Said, P. Juhas, R. Alonso-Mori, J. M. Glowina, A. Robert, J. Robinson, M. Sikorski, S. Song, M. Kozina, H. Lemke, L. Patthey, S. Owada, T. Katayama, M. Yabashi, Y. Tanaka, T. Togashi, J. Liu, C. Rayan Serrao, B. J. Kim, L. Huber, C.-L. Chang, D. F. McMorrow, M. Först, and J. P. Hill, Ultrafast energy- and momentum-resolved dynamics of magnetic correlations in the photo-doped Mott insulator Sr_2IrO_4 , *Nature Materials* **15**, 601 (2016).
- [18] D. G. Mazzone, D. Meyers, Y. Cao, J. G. Vale, C. D. Dashwood, Y. Shi, A. J. A. James, N. J. Robinson, J. Lin, V. Thampy, Y. Tanaka, A. S. Johnson, H. Miao, R. Wang, T. A. Assefa, J. Kim, D. Casa, R. Mankowsky, D. Zhu, R. Alonso-Mori, S. Song, H. Yavas, T. Katayama, M. Yabashi, Y. Kubota, S. Owada, J. Liu, J. Yang, R. M. Konik, I. K. Robinson, J. P. Hill, D. F. McMorrow, M. Först, S. Wall, X. Liu, and M. P. M. Dean, Laser-induced transient magnons in $\text{Sr}_3\text{Ir}_2\text{O}_7$ throughout the Brillouin zone, *Proceedings of the National Academy of Sciences* **118**, e2103696118 (2021), <https://www.pnas.org/doi/pdf/10.1073/pnas.2103696118>.
- [19] H. Lu, A. Gauthier, M. Hepting, A. S. Tremsin, A. H. Reid, P. S. Kirchmann, Z. X. Shen, T. P. Devereaux, Y. C. Shao, X. Feng, G. Coslovich, Z. Hussain, G. L. Dakovski, Y. D. Chuang, and W. S. Lee, Time-resolved rixs experiment with pulse-by-pulse parallel readout data collection using x-ray free electron laser, *Scientific Reports* **10**, 22226 (2020).
- [20] E. Paris, C. W. Nicholson, S. Johnston, Y. Tseng, M. Rumo, G. Coslovich, S. Zohar, M. F. Lin, V. N. Strocov, R. Saint-Martin, A. Revcolevschi, A. Kemper, W. Schlotter, G. L. Dakovski, C. Monney, and T. Schmitt, Probing the interplay between lattice dynamics and short-range magnetic correlations in CuGeO_3 with femtosecond RIXS, *npj Quantum Materials* **6**, 51 (2021).
- [21] E. M. Motoyama, G. Yu, I. M. Vishik, O. P. Vajk, P. K. Mang, and M. Greven, Spin correlations in the electron-doped high-transition-temperature superconductor $\text{Nd}_{2-x}\text{Ce}_x\text{CuO}_{4+\delta}$, *Nature* **445**, 186 (2007).
- [22] N. P. Armitage, P. Fournier, and R. L. Greene, Progress and perspectives on electron-doped cuprates, *Rev. Mod. Phys.* **82**, 2421 (2010).
- [23] K.-J. Xu, J. He, S.-D. Chen, Y. He, S. N. Abadi, C. R. Rotundu, Y. S. Lee, D.-H. Lu, Q. Guo, O. Tjernberg, T. P. Devereaux, D.-H. Lee, M. Hashimoto, and Z.-X. Shen, Anomalous normal-state gap in an electron-doped cuprate, *Science* **385**, 796 (2024), <https://www.science.org/doi/pdf/10.1126/science.adk4792>.
- [24] W. S. Lee, J. J. Lee, E. A. Nowadnick, S. Gerber, W. Tabis, S. W. Huang, V. N. Strocov, E. M. Motoyama, G. Yu, B. Moritz, H. Y. Huang, R. P. Wang, Y. B. Huang, W. B. Wu, C. T. Chen, D. J. Huang, M. Greven, T. Schmitt, Z. X. Shen, and T. P. Devereaux, Asymmetry of collective excitations in electron- and hole-doped cuprate superconductors, *Nature Physics* **10**, 883 (2014).
- [25] K. Ishii, M. Fujita, T. Sasaki, M. Minola, G. Dellea, C. Mazzoli, K. Kummer, G. Ghiringhelli, L. Braicovich, T. Tohyama, K. Tsutsumi, K. Sato, R. Kajimoto, K. Ikeuchi, K. Yamada, M. Yoshida, M. Kurooka, and J. Mizuki, High-energy spin and charge excitations in electron-doped copper oxide superconductors, *Nature Communications* **5**, 3714 (2014).
- [26] M. Hepting, L. Chaix, E. W. Huang, R. Fumagalli, Y. Y. Peng, B. Moritz, K. Kummer, N. B. Brookes, W. C. Lee, M. Hashimoto, T. Sarkar, J.-F. He, C. R. Rotundu, Y. S. Lee, R. L. Greene, L. Braicovich, G. Ghiringhelli, Z. X. Shen, T. P. Devereaux, and W. S. Lee, Three-dimensional collective charge excitations in electron-doped copper oxide superconductors, *Nature* **563**, 374 (2018).
- [27] A. S. Moskvina, True charge-transfer gap in parent insulating cuprates, *Phys. Rev. B* **84**, 075116 (2011).
- [28] J. H. Mentink, K. Balzer, and M. Eckstein, Ultrafast and reversible control of the exchange interaction in mott insulators, *Nature Communications* **6** (2015).
- [29] Y. Wang, Y. Chen, T. P. Devereaux, B. Moritz, and M. Mitrano, X-ray scattering from light-driven spin fluctuations in a doped mott insulator, *Communications Physics* **4** (2021).
- [30] K. Tsutsui, K. Shinjo, and T. Tohyama, Antiphase oscillations in the time-resolved spin structure factor of a photoexcited mott insulator, *Phys. Rev. Lett.* **126**, 127404 (2021).
- [31] F. Boschini, M. Zonno, E. Razzoli, R. P. Day, M. Michiardi, B. Zwartsenberg, P. Nigge, M. Schneider, E. H. da Silva Neto, A. Erb, S. Zhdanovich, A. K. Mills, G. Levy, C. Giannetti, D. J. Jones, and A. Damascelli, Emergence of pseudogap from short-range spin-correlations in electron-doped cuprates, *npj Quantum Materials* **5**, 6 (2020).
- [32] H. Padma, F. Gleran, S. F. R. TenHuisen, Z. Shen, H. Wang, L. Xu, J. D. Elliott, C. C. Homes, E. Skoropata, H. Ueda, B. Liu, E. Paris, A. Romaguera, B. Lee, W. He, Y. Wang, S. H. Lee, H. Choi, S.-Y. Park, Z. Mao, M. Calandra, H. Jang, E. Razzoli, M. P. M. Dean, Y. Wang, and M. Mitrano, Symmetry-protected electronic metastability in an optically driven cuprate ladder, *Nature Materials* **10.1038/s41563-025-02254-2** (2025).
- [33] G. Merzoni, L. Martinelli, S. Parchenko, S. F. R. TenHuisen, V. Lebedev, L. Adriano, R. Carley, N. Gerasimova, L. Mercadier, M. Teichmann, B. E. van Kuiken, Z. Yin, A. Alic, D. R. Baykusheva, S. G. Chiuzaibaian, S. D. Conte, O. Dogadov, A. Föhlisch, M. W. Haverkort, M. Kusch, T. Laarmann, W. S. Lee, M. M. Sala, Y. Y. Peng, Q. Z. Qiu, T. Schmitt, S. S. N. Lalithambika, S. Techert, G. Cerullo, M. Först, M. Mitrano, M. P. M. Dean, J. Schlappa, A. Scherz, and G. Ghiringhelli, Photo-generated charge-transfer excitons in nio revealed by ultrafast (2025), [arXiv:2504.16653 \[cond-mat.str-el\]](https://arxiv.org/abs/2504.16653).
- [34] D. Jost, E. G. Lomeli, T. Tang, J. J. Kas, J. J. Rehr, W.-S. Lee, H.-C. Jiang, B. Moritz, and T. P. Devereaux, Time-resolved x-ray spectroscopy from the atomic orbital ground state (2024), [arXiv:2405.16025 \[cond-mat.str-el\]](https://arxiv.org/abs/2405.16025).
- [35] D. R. Baykusheva, H. Jang, A. A. Husain, S. Lee, S. F. TenHuisen, P. Zhou, S. Park, H. Kim, J.-K. Kim, H.-D. Kim, *et al.*, Ultrafast renormalization of the on-site coulomb repulsion in a cuprate superconductor, *Phys. Rev. X* **12**, 011013 (2022).
- [36] A. V. Chumak, V. I. Vasyuchka, A. A. Serga, and B. Hillebrands, Magnon spintronics, *Nature Physics* **11**, 453 (2015).
- [37] J. S. *et al.*, The heisenberg-rixs instrument at the euro-

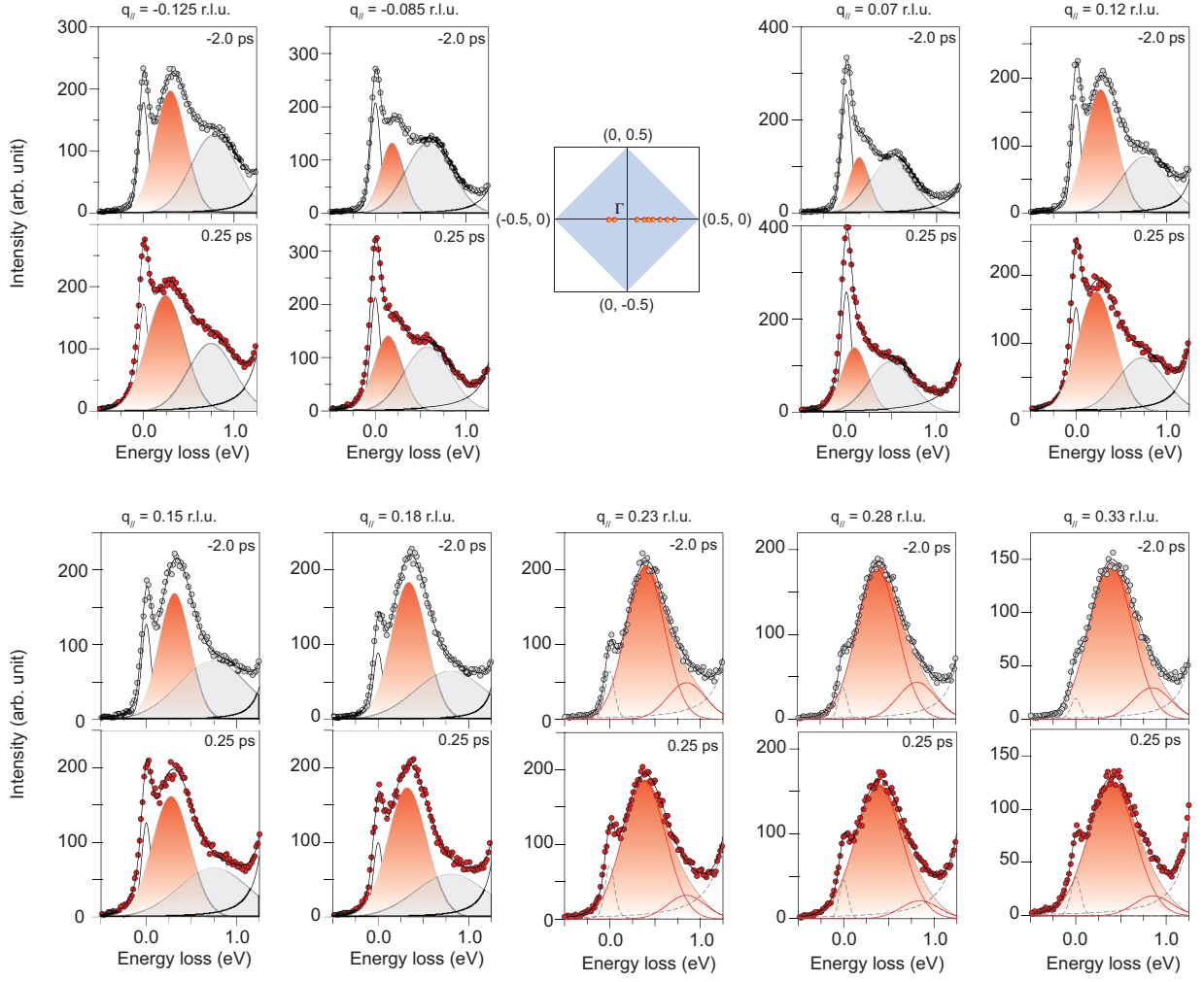
- pean xfel, *J. Syn. Rad* **32**, 29 (2011).
- [38] C. Jia, K. Wohlfeld, Y. Wang, B. Moritz, and T. P. Devereaux, Using rixs to uncover elementary charge and spin excitations, *Phy. Rev. X* **6**, 021020 (2016).
 - [39] R. B. Lehoucq, D. C. Sorensen, and C. Yang, *ARPACK Users' Guide: Solution of Large-scale Eigenvalue Problems with Implicitly Restarted Arnoldi Methods* (SIAM, 1998).
 - [40] C. Jia, Y. Wang, C. Mendl, B. Moritz, and T. Devereaux, Paradeisos: a perfect hashing algorithm for many-body eigenvalue problems, *Comput. Phys. Commun.* **224**, 81 (2018).
 - [41] S. R. Manmana, S. Wessel, R. M. Noack, and A. Muramatsu, Strongly correlated fermions after a quantum quench, *Phys. Rev. Lett.* **98**, 210405 (2007).
 - [42] K. Tsutsui, H. Kondo, T. Tohyama, and S. Maekawa, Resonant Inelastic X-ray Scattering Spectrum in High-Tc Cuprates, *Physica B: Condensed Matter* **284**, 457 (2000).
 - [43] S. Kourtis, J. van den Brink, and M. Daghofer, Exact diagonalization results for resonant inelastic x-ray scattering spectra of one-dimensional mott insulators, *Phys. Rev. B* **85**, 064423 (2012).
 - [44] L. J. Ament, G. Ghiringhelli, M. M. Sala, L. Braicovich, and J. van den Brink, Theoretical demonstration of how the dispersion of magnetic excitations in cuprate compounds can be determined using resonant inelastic x-ray scattering, *Phys. Rev. Lett.* **103**, 117003 (2009).
 - [45] L. Braicovich, J. van den Brink, V. Bisogni, M. M. Sala, L. J. P. Ament, N. B. Brookes, G. M. De Luca, M. Saluzzo, T. Schmitt, V. N. Strocov, and G. Ghiringhelli, Magnetic Excitations and Phase Separation in the Underdoped $\text{La}_{2-x}\text{Sr}_x\text{CuO}_4$ Superconductor Measured by Resonant Inelastic X-Ray Scattering, *Phys. Rev. Lett.* **104**, 077002 (2010).
 - [46] M. W. Haverkort, Theory of resonant inelastic x-ray scattering by collective magnetic excitations, *Phys. Rev. Lett.* **105**, 167404 (2010).
 - [47] H. C. Robarts, M. García-Fernández, J. Li, A. Nag, A. C. Walters, N. E. Headings, S. M. Hayden, and K.-J. Zhou, Dynamical Spin Susceptibility in La_2CuO_4 Studied by Resonant Inelastic X-ray Scattering, *Phys. Rev. B* **103**, 224427 (2021).



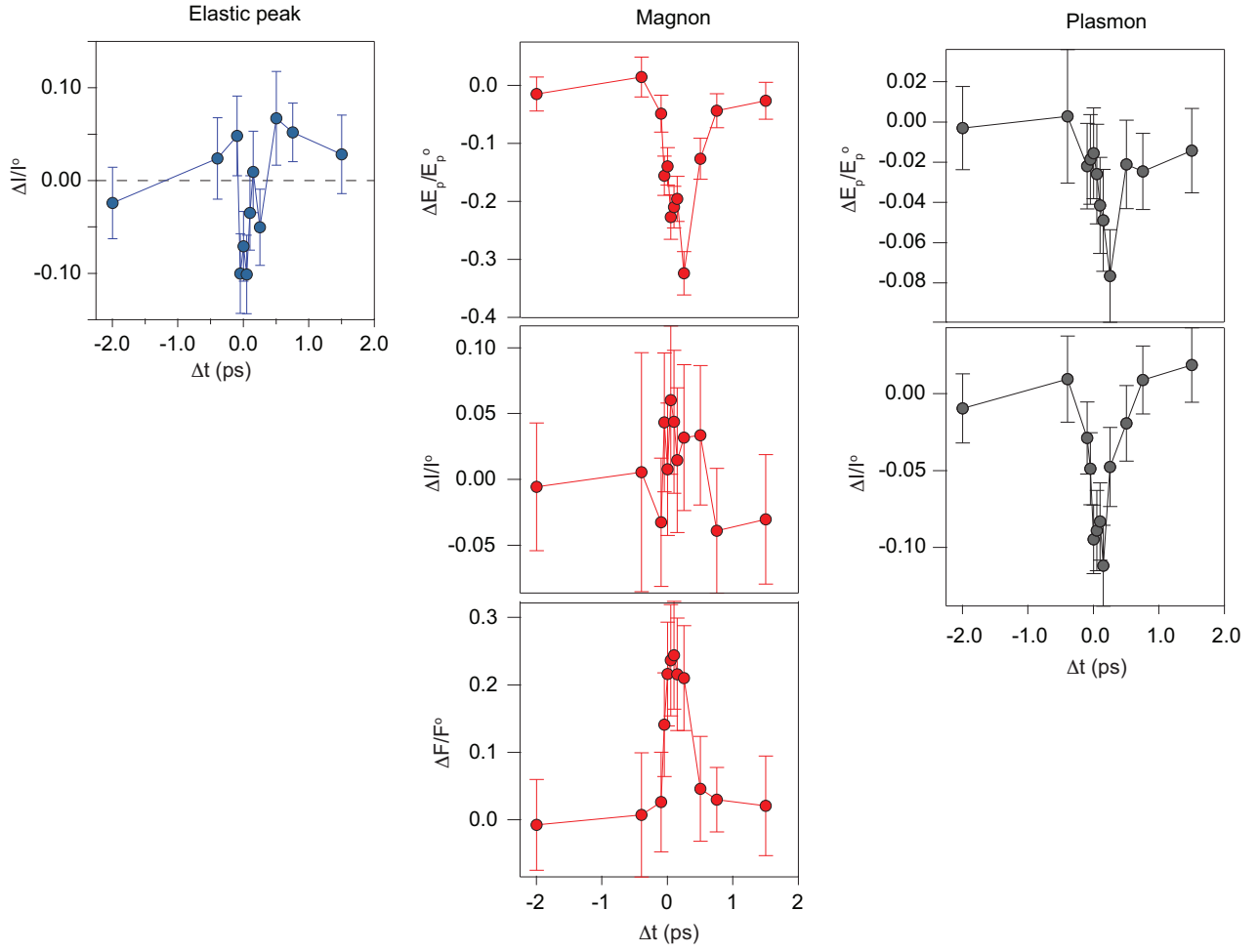
Extended Data Fig. 1. **Scattering and Pump-probe Geometry and NCCO reflectivity to 400 nm.** **a.** k_{in} and k_{out} represent the momenta of the incident and outgoing x-ray, respectively. The scattering angle is 125° . The ac plane of the crystal is in the scattering plane, as sketched. q and $q_{||}$ represent the magnitude of the momentum transfer and the projected in-plane momentum along the a-axis (i.e. h -direction). The $q_{||}$ is defined to be positive when $\theta > 62.5^\circ$ (i.e. on the branch of grazing x-ray emission). The polarization of the incident x-ray lies in the scattering plane (i.e. π polarization). The 400 nm pump is collinear with the incident x-ray with a σ polarization **b.** Angle-dependent reflectivity for σ - and π -polarized 400 nm light. α_i denotes the angle-of-incidence as measured from the surface normal. Global fits of the Fresnel equations are shown as solid lines. Dashed lines are extrapolation of the fits.



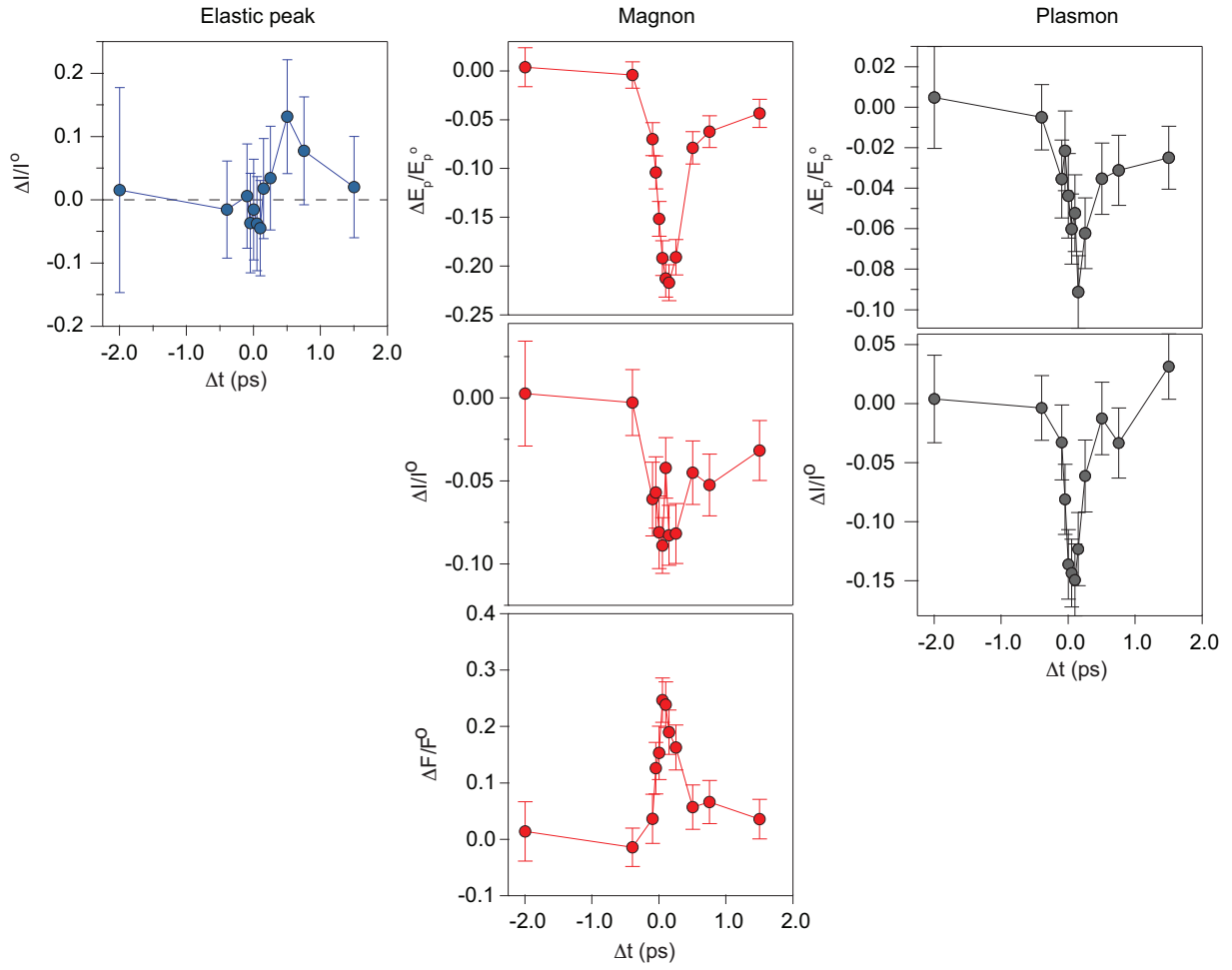
Extended Data Fig. 2. **Illustration of energy gain spectrum in thermal equilibrium condition.** When a finite population of bosonic modes exists, anti-Stokes scattering becomes detectable, resulting in an energy gain spectral weight in the dynamical structure factor ($S(q, \omega)$), which can be measured using inelastic neutron and X-ray scattering experiments. In the thermal equilibrium condition, modes are excited by thermal energy with a population following the Bose-Einstein statistics. Using the dissipation-fluctuation theorem, $S(q, \omega) = (1 + n(\omega, T)) \cdot \chi(q, \omega)''$, where $n(\omega, T)$ and $\chi(q, \omega)''$ are the Bose-Einstein distribution function and dynamical susceptibility $\chi(q, \omega)''$, respectively. In this simulation, we use the damped harmonic oscillator function to generate $\chi(q, \omega)''$ for three different scenarios: a sharp mode (**a**, $\omega > 2\Gamma$), a damped mode ($\omega \sim 2\Gamma$), and an overdamped mode ($\omega < 2\Gamma$). Only in the situation of a sharp mode, a distinct peak can be resolved in the energy gain spectrum, which is the commonly known anti-Stoke peak. In the situations of a broad mode (**b**, **c**), the anti-Stoke peak is not resolvable, instead the $S(q, \omega)$ manifests as a broadened peak with significant spectral weight in the negative energy loss (energy gain). Regarding the case of photoexcitation, the dissipation-fluctuation theorem cannot be applied due to the non-equilibrium nature near time zero. Nevertheless, we expect a qualitative similarity for the spectral lineshape in the presence of photo-excited mode population. Since the paramagnon and plasmon are heavily damped in the optimally-doped electron-doped cuprates, we believe that a Gaussian function is a realistic and simplest model to fit the time dependence of the paramagnon and plasmon.



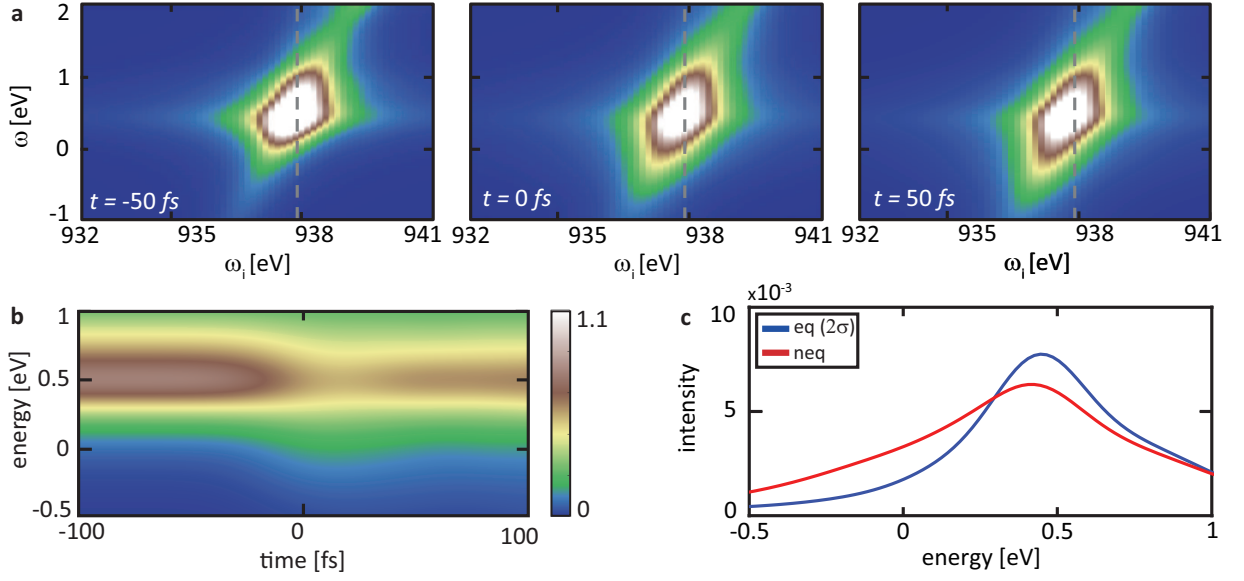
Extended Data Fig. 3. **Raw RIXS data and fitting.** Raw data (markers) used for momentum dependence analysis in Figs. 2, and 3 are shown here. The fitted curves generated from the minimal model described in **Methods** are superimposed as black curves. The red and black shaded peaks represent the fitted paramagnon and plasmon excitations, respectively. We note that for $q_{\parallel} \geq 0.23$ r.l.u., the paramagnon cannot be described by a single Gaussian peak to the slight asymmetry in the RIXS lineshape. To account for spectral weight of the entire paramagnon peak, an additional Gaussian peak is included at high energy.



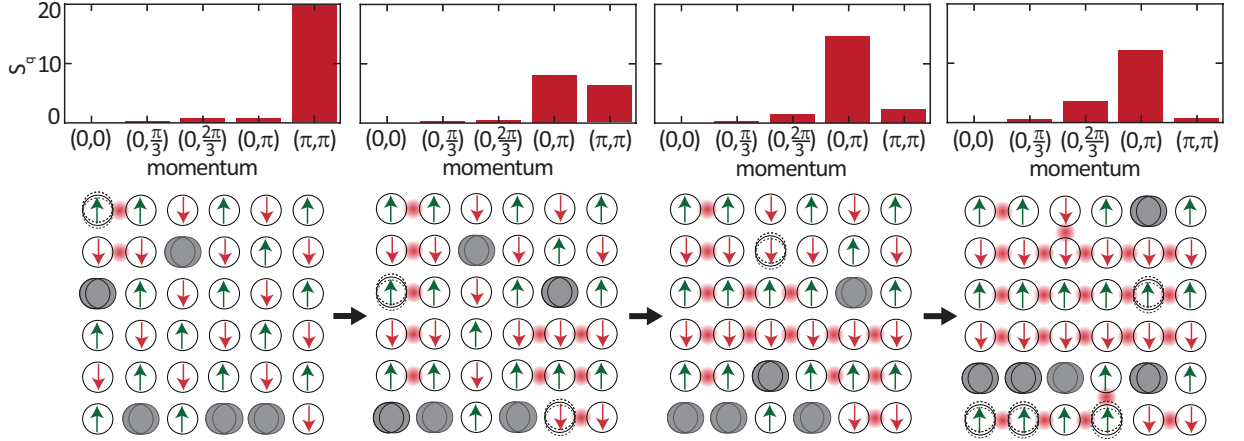
Extended Data Fig. 4. **Fitted parameters of $q_{||} = -0.085$ r.l.u. data.** All fitted parameters for the $q_{||} = -0.085$ r.l.u. data shown in Fig. 5a-c. We found that if the plasmon width was used as a fitting parameter for the spectra after time zero, it decreases, which we believe is not physical. Thus, the width of the plasmon was first determined in the spectrum before time zero ($\Delta t = -2.0$ ps); then it was kept fixed for spectra at later time delays.



Extended Data Fig. 5. **Fitted parameters of $q_{||} = -0.125$ r.l.u. data.** All fitted parameters for the $q_{||} = -0.125$ r.l.u. data shown in Fig. 5d-f. We found that if the plasmon width was used as a fitting parameter for the spectra after time zero, it decreases, which we believe is not physical. Thus, the width of the plasmon was first determined in the spectrum before time zero ($\Delta t = -2.0$ ps); then it was kept fixed for spectra at later time delays.



Extended Data Fig. 6. **Exact Diagonalization time-resolved RIXS calculations** a. Snapshots of the trRIXS spectra at $q = (0.67, 0)$ for the system before the pump, at the pump center, and after its departure. The dashed line indicates the resonance incident energy ω_i . b. Time evolution of the RIXS scattering cross section by fixing the incident energy at $\omega_i = 5.12$ eV. c. Spectral cuts of trRIXS before and at the center of the pump.



Extended Data Fig. 7. **Spin scrambling due to doublon motion.** Initially, the system exists in a near antiferromagnetic state characterized by alternating electron spins forming an ordered pattern. The movement of a doublon (grey) disrupts this order, leading to a ‘scrambling’ of the spins. As the doublon continues to move, the scrambling effect intensifies and further disrupts the order of the system. Above the lattice, a plot of $S(q)$ varying momentum illustrates a shift from large to small momentum, correlating with increased spin scrambling.